

The Challenge of Ovarian Cancer: Steps Toward Early Detection Through Advanced Signal Processing in Magnetic Resonance Spectroscopy

Karen Belkić MD PhD^{1,2,3} and Dževad Belkić PhD¹

¹Department of Oncology-Pathology Karolinska Institute and Medical Radiation Physics and Nuclear Medicine, Karolinska Hospital, Stockholm, Sweden

²School of Community and Global Health, Claremont Graduate University, Claremont, California, USA

³Institute for Prevention Research, Keck School of Medicine, University of Southern California, Alhambra, California, USA

ABSTRACT: Ovarian cancer is a major cause of cancer death among women worldwide, and particularly in Israel. Although the disease at stage IA has 5 year survival rates of over 90%, early detection methods are not sufficiently accurate. Consequently, ovarian cancer is typically diagnosed late, which results in high fatality rates. An excellent candidate for early ovarian cancer detection would be *in vivo* magnetic resonance spectroscopy (MRS) because it is non-invasive and free of ionizing radiation. In addition, it potentially identifies metabolic features of cancer. Detecting these metabolic features depends on adequate processing of encoded MRS time signals for reconstructing interpretable information. The conventional Fourier-based method currently used in all clinical scanners is inadequate for this task. Thus, cancerous and benign ovarian lesions are not well distinguished. Advanced signal processing, such as the fast Padé transform (FPT) with high-resolution and clinically reliable quantification, is needed. The effectiveness of the FPT was demonstrated in proof-of-concept studies on noise-controlled MRS data associated with benign and cancerous ovaries. The FPT has now been successfully applied to MRS time signals encoded *in vivo* from a borderline serous cystic ovarian tumor. Noise was effectively separated out to identify and quantify genuine spectral constituents that are densely packed and often overlapping. Among these spectral constituents are recognized and possible cancer biomarkers including phosphocholine, choline, isoleucine, valine, lactate, threonine, alanine, and myoinositol. Most of these resonances remain undetected with Fourier-based *in vivo* MRS of the ovary. With Padé optimization, *in vivo* MRS could become a key method for assessing ovarian lesions, more effectively detecting ovarian cancer early, thereby improving survival for women afflicted with this malignancy.

IMAJ 2017; 19: 517–525

KEY WORDS: ovarian cancer, early detection, magnetic resonance spectroscopy (MRS), signal processing, *BRCA* mutations

THE CURRENT CHALLENGE OF OVARIAN CANCER

Among women worldwide, ovarian cancer is the 8th most common cause of cancer mortality, with approximately 158,000 deaths in 2013 alone [1]. In Israel the age-standardized mortality rate for ovarian cancer in 2012 was 5.21 per 100,000 women, which is higher than in the United States, Canada, and the European Union [2]. Compared to Israeli Arab women and women from other Middle East Cancer Consortium countries, Israeli Jewish women have the highest age-standardized incidence of ovarian cancer [3]. Among Ashkenazi Jewish women in Israel, up to 40% of the ovarian cancer risk is due to *BRCA1* or *BRCA2* gene mutations [4]. When detected early, ovarian cancer has an excellent prognosis. At stage IA (confined to a single ovary), the 5 year survival rates are over 90% [5]. However, the majority of ovarian cancers are detected late, at stage III or IV with spread outside the true pelvis, and mortality rates are high [6]. The challenge is that early stage ovarian cancer is often asymptomatic and the ovary may be of normal size [7]. Once symptoms appear, the disease is often already advanced. Symptom-triggered diagnostic workups do not significantly aid early diagnosis [8].

The most widely used ovarian cancer screening methods are transvaginal ultrasound (TVUS) and serum cancer antigen (CA-125). Although some evidence from the United Kingdom may indicate the contrary [9], the consensus from large randomized trials is that using CA-125 and TVUS to screen for ovarian cancer in asymptomatic women does not reduce mortality nor contribute to earlier ovarian cancer detection and are associated with a large percentage of false positives [10]. The latter have harmful consequences, including that many women undergo surgical removal of benign ovarian lesions. For women not clearly at high risk, the harm of routine screening for ovarian cancer is considered to outweigh the benefits [11]. For women at high ovarian cancer risk, screening with CA-125 and TVUS is often performed, but without prospective evidence that this leads to early detection [12,13].

Currently, the most effective means of reducing ovarian cancer risk in women who are carriers of deleterious *BRCA* muta-

tions is bilateral salpingo-oophorectomy, recommended by the National Comprehensive Cancer Network for women 35–40 years of age who have completed childbearing [14]. Adherence to this recommendation has been nearly 100% among women over age 40 attending a dedicated multi-disciplinary follow-up clinic for *BRCA* gene mutation carriers at the Rabin Medical Center, Petah Tikva, Israel [15]. Although salpingo-oophorectomy does reduce cancer risk, complex physical and psychosocial issues arise that are associated with “mutilation of a healthy organ, termination of fertility, self-wounding, and castration” [16].

CONTINUED SEARCH FOR EFFECTIVE, NON-INVASIVE SCREENING METHODS

Concerns for women at known high risk and for the overall population have motivated a search for non-invasive methods to detect ovarian cancer early. Biomarkers other than CA-125 have been investigated, but none improve diagnostic accuracy enough to recommend use for routine screening [17]. Magnetic resonance imaging (MRI) helps distinguish benign from malignant ovarian lesions that are indeterminate on TVUS [18,19], but nearly one-quarter of benign ovarian lesions were misdiagnosed as cancerous using TVUS plus MRI [19]. Diffusion-weighted imaging (DWI) helps assess adnexal lesions, but many false positives also occur with DWI [20].

THE POTENTIAL OF MOLECULAR IMAGING THROUGH MAGNETIC RESONANCE SPECTROSCOPY

Through magnetic resonance spectroscopy (MRS), it is possible to go beyond anatomy to assess the metabolic features of tissues. Via MRS, molecular changes characterizing the cancer process, the “hallmarks of cancer,” can potentially be uncovered [21]. We performed a meta-analysis [22] of the published studies applying in vivo MRS to 134 malignant and 114 benign ovarian lesions plus three borderline lesions, with encoding performed via clinical (1.5 or 3T) magnetic resonance (MR) scanners. The MRS time signals were processed by the fast Fourier transform (FFT) with eventual post-processing via fitting. At a resonant frequency of ~1.3 parts per million (ppm), a lactate doublet peak reflecting anaerobic glycolysis and lipid were sometimes identified. Other peaks that were sometimes detected included creatine at 3.0 ppm, which is a marker of energy metabolism, and choline at 3.2 ppm, or total choline from 3.14 to 3.34 ppm, which is a marker of membrane damage, cellular proliferation, and cell density that reflects phospholipid metabolism of cell membranes. A peak resonating at ~2.0 ppm was occasionally detected which, according to in vitro analysis, is comprised of N-acetyl aspartate (NAA) and N-acetyl groups from glycoproteins or glycolipids [23]. Only choline and lactate

Because of late detection, ovarian cancer is a major cause of cancer death in women

were significantly detected more often in malignant lesions. Yet, relying on choline detection alone, 50 benign lesions would have been wrongly classified as malignant (i.e., false positive results) with positive predictive value (PPV) of 66%. Twenty cancerous ovarian lesions would have been erroneously considered benign based on lack of detected choline,

resulting in false negative findings: negative predictive value (NPV) of 57.4%. Adjustment for

age and magnetic field strength, B_0 , provided a stronger model for choline, but with markedly fewer patients. Lactate yielded better PPV and NPV, but data were available for only 25% of patients. An adjusted model with lactate and choline with 50 patients yielded the best PPV, NPV, and overall accuracy, but 4 of 26 patients with benign ovarian lesions were predicted to have ovarian cancer and 4 of 24 patients with ovarian cancer were predicted to have benign lesions. From this meta-analysis, we conclude that in vivo MRS with conventional Fourier-based processing did not sufficiently distinguish cancerous and benign ovarian lesions [22]. Through in vitro MRS using analytical chemistry methods with stronger static magnetic fields, more metabolic insight is gleaned to distinguish malignant from benign ovarian lesions. Comparing fluid from 12 cancerous and 23 benign ovarian cysts showed significantly higher concentrations of choline, lactate, isoleucine (1.02 ppm), valine (1.04 ppm), threonine (1.33 ppm), alanine (1.51 ppm), lysine (1.67–1.78 ppm), methionine (2.13 ppm), and glutamine (2.42–2.52 ppm) in malignant fluid [24]. With gas chromatography-mass spectrometry of ovarian cyst fluid [25], NAA was found in high concentrations in ovarian serous cystadenocarcinomas. An in vitro MRS study of cells from ovarian cancer and benign ovary indicated significantly higher intracellular lactate in ovarian cancer cells [26]. Comparing human epithelial ovarian carcinoma cell lines with normal or immortalized ovarian epithelial cells, phosphocholine at ~3.22 ppm was three- to eightfold higher in the cancer cells [27]. Notably, phosphocholine is recognized as a biomarker of malignant transformation [28].

UNREALIZED POTENTIAL DUE TO INADEQUATE PROCESSING OF MAGNETIC RESONANCE SPECTROSCOPY TIME SIGNALS ENCODED IN VIVO

In vitro findings indicate that ovarian cancer diagnostics could be enhanced via MRS. However, this potential has not been realized for in vivo MRS. The main reason is that MRS data have not been adequately analyzed. Without mathematical processing, MRS time signals, or free induction decays (FIDs) are uninterpretable. Thus, for metabolite profiling, encoded MRS time signals are converted into a spectral representation in the frequency domain, as done in clinical

If detected early, ovarian cancer has an excellent prognosis, justifying the search for effective screening methods

MR scanners by the FFT. This qualitative method has low resolution, and being non-parametric, can generate only a total shape spectrum (envelope). Quantitative information regarding the metabolites present in a given tissue cannot be ascertained by the FFT alone.

ADVANCED SIGNAL PROCESSING FOR MAGNETIC RESONANCE SPECTROSCOPY DATA FROM THE OVARY

An advanced signal processor, the fast Padé transform (FPT), defined by the unique ratio of two polynomials P_K/Q_K of degree K , has high-resolution capacity and is quantification-equipped [29,30]. Here, K is the model order, indicating the predicted number of resonances associated with metabolites present in the scanned tissue. The quotient P_K/Q_K represents a complex-valued spectrum extracted directly and uniquely from the encoded FID points. For interpretation, the real part of P_K/Q_K is used. The independent variable in P_K/Q_K is a harmonic given by a complex frequency-dependent damped exponential. Signal processing by the FPT can be non-parametric (to generate spectral envelopes) or parametric (for quantification). The former is accomplished as soon as P_K/Q_K becomes available. For the latter, the roots of the characteristic equations $P_K = 0$ and $Q_K = 0$ are determined to reconstruct the complex frequencies and amplitudes. The high resolution of spectra by the FPT is due to its extrapolation and interpolation capabilities, plus nonlinearity which aids noise suppression.

INITIAL PROMISING RESULTS OF THE FAST PADÉ TRANSFORM ON NOISE-CONTROLLED MAGNETIC RESONANCE SPECTROSCOPY DATA FROM THE OVARY

In proof-of-concept studies, the FPT was shown to be optimally qualified to handle MRS time signals from the ovary [31-33]. Belkić and Belkić [31] applied the FPT to synthesized noiseless FIDs associated with MRS data reported by Boss et al. [24] for benign and cancerous ovarian cyst fluid. With only 64 signal points, the FPT resolved all of the resonances, including the closely lying isoleucine and valine, accurately computing all 12 metabolite concentrations. For comparison, we also applied the FFT to these ovarian cyst data. With 64 signal points, crude and uninterpretable spectra were generated by the FFT. The FFT required 8192 signal points to roughly resolve the 12 resonances, with a formidable 32,768 signal points needed for convergence of Fourier envelopes. These results showed the superior resolving power of the FPT. With added noise of progressively higher levels [32,33], the capability of the FPT to resolve and precisely quantify all the resonances associated with MRS data for benign and cancerous ovarian cyst fluid was confirmed. Further studies performed on noise-controlled MRS data from other tissues also showed that the FPT accurately analyzed MRS time signals,

yielding quantitative information for a large number of metabolites from cancerous, benign and/or normal brain, breast, and prostate tissue [22,30]. From these proof-of-concept studies, as well as from successful application of the FPT to in vivo MRS of the brain [30,34,35], we concluded that Padé-optimized in vivo MRS should be applied where the greatest added value is anticipated. This expected added value is for ovarian cancer diagnostics, where the need for an effective in vivo MRS-based screening method has been highlighted for almost two decades [12,36], but with the realization still pending.

PADÉ-OPTIMIZATION FOR MAGNETIC RESONANCE SPECTROSCOPY TIME SIGNALS ENCODED IN VIVO FROM THE OVARY

Belkić and Belkić [22] applied the FPT to MRS time signals encoded in vivo from a cystic ovarian tumor on a 3T MR scanner from a 56 year old patient with an enlarged left ovary [23]. The time signals were provided by our colleagues at the Department of Obstetrics & Gynecology, Radboud Medical Center, the Netherlands. A Siemens 3T Magnetom Tim Trio

MR scanner (Siemens AG, Erlangen, Germany) was used to encode the time signals, which contained 1024 complex data points. The bandwidth (BW) was 1200 Hz, sampling time $\tau = 0.833$ ms ($\tau = 1/BW \approx 0.833$ ms)

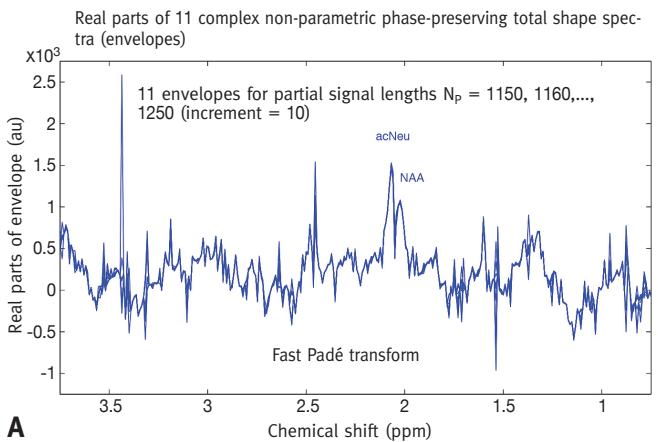
Via the advanced signal processor, the fast Padé transform, metabolic markers associated with ovarian cancer can be identified and reliably quantified through in vivo magnetic resonance spectroscopy to aid early detection of ovarian cancer

and the number of excitations (NEX) equal to 128. A point-resolved spectroscopy sequence was used for single-voxel MRS. Water was partially suppressed via WET (water suppression through enhanced T_1 effects). After in vivo MRS encoding, the tumor was surgically excised and histopathologic analysis revealed a borderline serous cystic lesion [23]. Two echo times (TE) of 30 and 136 ms were used [23], both with repetition time of 2000 ms. Our analysis used the encoding at TE = 30 ms with richer extractable metabolic information. Better resolution was provided by the FPT compared to total shape spectra generated by the FFT applied to the MRS time signals encoded in vivo. This finding [22] supports the benchmarking studies [30-33] in which the high-resolution capabilities of the FPT were shown. The Regional Ethics Committee, Karolinska Institute (Dnr # 2007/708-31/1) found no ethical issues to preclude implementation of this research.

SPECTRA AVERAGING BY THE NON-PARAMETRIC FAST PADÉ TRANSFORM FOR NOISE SUPPRESSION: GENERATING “CLEAN” ENVELOPES

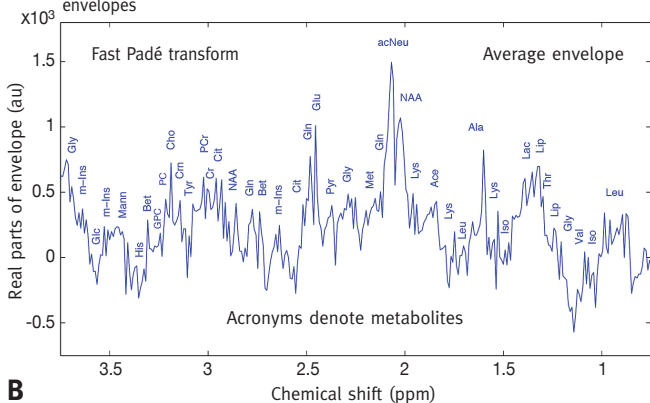
A major problem with in vivo encoded MRS is related to noise from the encoding plus from unphysical resonances that arise in data reconstruction by any processor [32,35]. Noise-like spikes result, as shown in Figure 1A, for the real parts of 11 complex envelopes reconstructed non-parametrically by the FPT at partial signal lengths $N_P = 1150, 1160, \dots, 1250$. A spike

Figure 1. In vivo MRS for ovarian tumor: Spectra averaging for strong suppression of noise. Real parts of 11 complex envelopes for partial signal lengths $N_p = 1150, 1160, \dots, 1250$, reconstructed by the non-parametric FPT, using the MRS time signal encoded in vivo from a borderline serous cystic ovarian lesion [23], as shown in [A]. The 11 complex envelopes are averaged, and the real part of that average is shown in [B]



A

Use of FID data encoded at $B_0 = 3T$, $TE = 30$ ms, $TR = 2$ s, $BW = 1.2$ kHz, $NEX = 128$
 No noisy spikes as the most important advantage of the arithmetic average envelope:
 Real part of the complex average envelope from 11 complex non-parametric envelopes



B

Au = arbitrary units, FPT = fast Padé transform, MRS = magnetic resonance spectroscopy, FID = free induction decays, TE = echo times, TR = repetition time, BW = bandwidth, NEX = number of excitations, ppm = parts per million (metabolite abbreviations above the peaks: Ace = acetic acid, AcNeu = N-acetylneuraminic acid, Ala = alanine, Bet = betaine, Cho = choline, Cit = citrate, Cr = creatine, Crm = creatinine, Glc = glucose, Gln = glutamine, Glu = glutamate, Gly = glycine, GPC = glycerophosphocholine, His = histidine, Iso = isoleucine, Lac = lactate, Leu = leucine, Lip = lipid, Lys = lysine, Mann = mannose, Met = methionine, m-Ins = myoinositol, NAA = N-acetyl aspartate, PC = phosphocholine, PCr = phosphocreatine, Pyr = pyruvate, Tyr = tyrosine, Val = valine)

identified. Beginning from ~ 0.94 ppm, a doublet and triplet of leucine are seen. In the valley thereafter are isoleucine and valine. Glycine follows on the upturn at ~ 1.2 ppm. Next is lipid, and then threonine. On a prominence at ~ 1.3 ppm are lipid and a lactate doublet. A depression follows with an isoleucine multiplet at ~ 1.48 ppm and a lysine multiplet with a prominent peak at ~ 1.52 ppm. Next is an alanine doublet with the first peak quite tall. Another valley follows with two leucine peaks at ~ 1.73 ppm, and then lysine. Next, a small acetic acid doublet and a lysine doublet appear, bordering with NAA. Several peaks (glutamine, methionine, glycine, and pyruvate) follow to the left of AcNeu, and then the large glutamate and glutamine peaks appear at ~ 2.45 ppm. On the left side is a small citrate peak, a myoinositol triplet at ~ 2.6 ppm, and then betaine, glutamine, NAA, and citrate peaks. A small creatine peak at 3.0 ppm is seen, to its left is phosphocreatine, a small tyrosine multiplet and a creatinine peak. A choline peak appears at 3.2 ppm, a smaller phosphocholine at ~ 3.22 ppm, and an even smaller glycerophosphocholine peak thereafter. A betaine peak follows at ~ 3.27 ppm, then histidine, mannose, and a myoinositol multiplet. A small glucose peak appears at ~ 3.54 ppm, and then a myoinositol multiplet and a glycine peak.

COMPONENT SPECTRA RECONSTRUCTED BY THE PARAMETRIC FAST PADÉ TRANSFORM

Figure 1 confirms that spectra averaging stabilizes envelopes against over-sensitivity to changes in model order K , but we do not end signal processing with shape estimation. The purpose of MRS is to provide quantitative information about resonant frequencies (chemical shifts), relaxation times T_2^* , signal amplitudes and metabolite concentrations. Chemical shifts inform about electronic shielding of protons bound in different molecules. Proton spin-spin coupling is reflected in T_2^* . Absolute values (magnitudes) of complex amplitudes reflect the abundance of resonating protons, as the main determinants of metabolite concentrations. The parametric FPT first reconstructs the fundamental frequencies and amplitudes, with component spectra generated subsequently, in two different modes. In Figure 2A the real part of the complex average envelope [Figure 1B] is replotted. That complex average envelope is inverted to generate a new MRS time signal to which the FPT is applied at a fixed N_p . The partial signal length used was $N_p = 1300$, $K = 650$, where $N_p = 2K$. Thus, K is greater than the model orders $K = 575, 580, \dots, 625$ from which the 11 envelopes from Figure 1A were reconstructed. Insofar as convergence of spectral parameters is achieved, as is presently the case, quantification is found to be insensitive to the choice of interval for model order K [37]. The first complex mode, termed "usual," with the real parts of these components shown in Figure 2B, is very dense, with both absorption and dispersion spectra visualized. The reason for this mixture of absorption and dispersion spectra is that the amplitudes are complex-valued, with their phases being non-

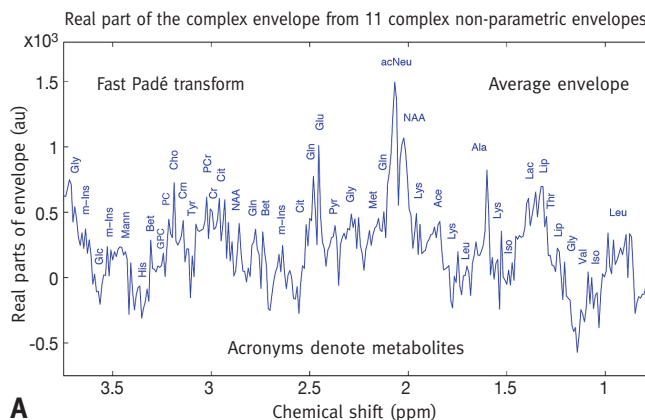
at ~ 3.4 ppm is the largest structure therein, with many other prominent spikes intermingled throughout the spectral range of interest (SRI): 0.75-3.75 ppm. Taking the average of the 11 complex envelopes, an average complex envelope is generated, the real part of which is shown in Figure 1B. Therein, the noisy spikes have disappeared and only genuine peaks remain. The largest peaks are N-acetylneuraminic acid (acNeu) at 2.06 ppm and NAA at 2.03 ppm. Many other resonances can be

zero. Many insights can be gleaned from the usual component spectra. In the chemical shift region ~1.3 ppm, two lipid resonances in the dispersion mode with large positive and negative lobes are prominent. The threonine and lactate resonances are small in the usual component spectra and, on the total shape spectrum, are serrations jutting above the prominence, which is mainly due to a lipid. On the usual component spectra of Figure 2B, NAA appears larger than acNeu because acNeu is in the dispersion mode, with a narrow positive and prominent negative lobe. Its peak height is lower than if it were in the pure absorption mode. In contrast, NAA is almost in the absorption mode. In the envelope from Figure 2A, the situation is the opposite, the acNeu peak is taller than NAA due to more constructive interference for acNeu than for NAA. Large, wide resonances in the dispersion mode are also seen from ~3.45–3.75 ppm due to macromolecules causing baseline oscillations in the total shape spectrum. The "ersatz" component spectra provide another way to distinguish closely overlapping resonances, with their phases set to zero to remove interference effects. All resonances then become purely absorptive Lorentzian functions. In Figure 3B, the real parts of the ersatz component spectra are shown. Figure 3A shows the average envelope. The ersatz mode helps visualize overlap of closely lying or hidden resonances. The lipid resonances centered at 1.3 ppm appear as larger, symmetrical Lorentzians functions, under which the lactate and threonine doublets are seen. The acNeu peak appears taller than NAA. With the phase removed from the amplitude, the right negative lobe of acNeu merges with the left positive lobe. Over 90 peaks are identified with ersatz component spectra in the shown SRI. Notwithstanding the clarity provided by ersatz spectra, there is a caveat: the heights of the ersatz peaks do not reflect the actual abundance of metabolites. The number of component resonances is the same in the usual and ersatz modes, but their full widths at half maximum (FWHM) are not equal. Thus, the peak areas of a given component differ in the usual and ersatz modes. Whenever the phases are non-zero, interference effects must be taken into account, and the usual components with complex amplitudes should be used to compute metabolite concentrations.

THE PADÉ-BASED FEATURE OF UNEQUIVOCAL SIGNAL-NOISE SEPARATION

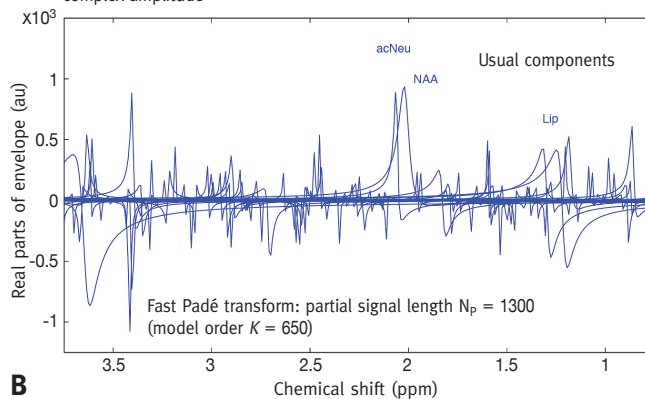
A critical obstacle in MRS is noise mixed with the encoded FIDs. Subsequent data analysis must separate true information from false. Signal processing exacerbates the already difficult situation by adding more noise, simultaneously generating genuine and spurious resonances. This problem is solved by the FPT through signal-noise separation (SNS): all information that is incoherent with the true physical part of the processed data is identified and discarded. Algorithmically, SNS is accomplished through the stability test of the reconstructed spectral parameters as a function of model order *K*. Stable reconstructed frequencies and

Figure 2. In vivo MRS for ovarian tumor: Average envelope and usual components (non-zero phases). The time signal or FID from inversion of the complex average envelope, whose real part is shown in [A] is subjected to the parametric FPT to generate the usual component spectra in [B], where absorption and dispersion line shapes are mixed



A

Complex average envelope is inverted to generate a new time signal or FID which is quantified by the fast Padé transform giving the usual components: Real parts of usual component spectra with non-zero values of phases of complex amplitude

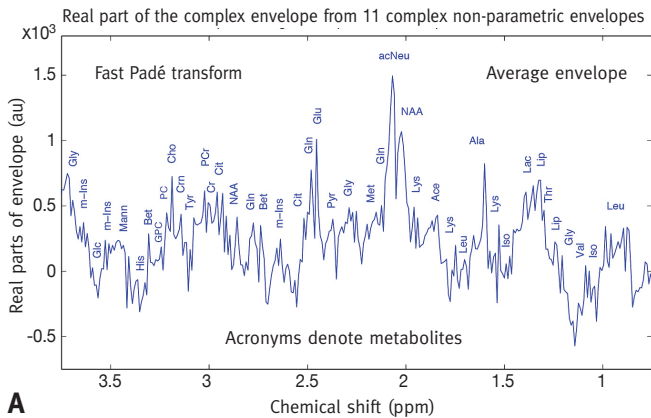


B

Au = arbitrary units, FPT = fast Padé transform, MRS = magnetic resonance spectroscopy, FID = free induction decays, TE = echo times, TR = repetition time, BW = bandwidth, NEX = number of excitations, ppm = parts per million (metabolite abbreviations above the peaks: Ace = acetic acid, AcNeu = N-acetylneuraminic acid, Ala = alanine, Bet = betaine, Cho = choline, Cit = citrate, Cr = creatine, Crn = creatinine, Glc = glucose, Gln = glutamine, Glu = glutamate, Gly = glycine, GPC = glycerophosphocholine, His = histidine, Iso = isoleucine, Lac = lactate, Leu = leucine, Lip = lipid, Lys = lysine, Mann = mannose, Met = methionine, m-Ins = myoinositol, NAA = N-acetyl aspartate, PC = phosphocholine, PCr = phosphocreatine, Pyr = pyruvate, Tyr = tyrosine, Val = valine)

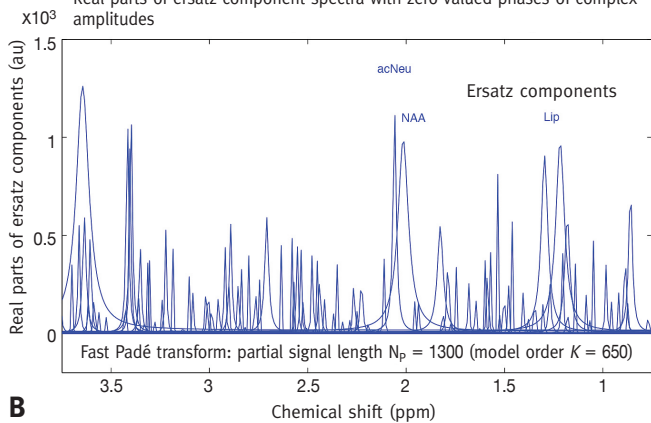
amplitudes are binned as genuine and retained. Unstable parameters are categorized as spurious and are removed. Along with instability, spurious resonances show pole-zero coincidence, negative FWHM, and zero-amplitude. The poles and zeros of the spectrum P_K/Q_K in the FPT are the roots of the characteristic equations, $Q_K = 0$ and $P_K = 0$ respectively. Both sets of these *K* roots give complex frequencies. The real and imaginary parts of frequencies from $Q_K = 0$ are the chemical shifts and the reciprocal of relaxation times T_2^* , respectively. The signal amplitudes are the complex Cauchy residues of the spectrum P_K/Q_K taken

Figure 3. In vivo MRS of envelope and ersatz components (zero phases)
 The time signal or FID from inversion of the complex average envelope, whose real part is shown in **[A]** is subjected to the FPT to generate the ersatz component spectra in **[B]**, all in the absorption mode with numerous closely-overlapping positively-oriented resonances



A

Complex average envelope is inverted to generate a new time signal or FID, which is quantified by the fast Padé transform giving the ersatz components: Real parts of ersatz component spectra with zero-valued phases of complex amplitudes



B

Au = arbitrary units, FPT = fast Padé transform, MRS = magnetic resonance spectroscopy, FID = free induction decays, TE = echo times, TR = repetition time, BW = bandwidth, NEX = number of excitations, ppm = parts per million (metabolite abbreviations above the peaks: Ace = acetic acid, AcNeu = N-acetylneuraminic acid, Ala = alanine, Bet = betaine, Cho = choline, Cit = citrate, Cr = creatine, Crm = creatinine, Glc = glucose, Gln = glutamine, Glu = glutamate, Gly = glycine, GPC = glycerophosphocholine, His = histidine, Iso = isoleucine, Lac = lactate, Leu = leucine, Lip = lipid, Lys = lysine, Mann = mannose, Met = methionine, m-Ins = myoinositol, NAA = N-acetyl aspartate, PC = phosphocholine, PCr = phosphocreatine, Pyr = pyruvate, Tyr = tyrosine, Val = valine)

poles and zeros, and non-zero amplitudes. Froissart doublets automatically annihilate in the spectrum P_K/Q_K , since poles from Q_K that coincide with zeros of P_K cancel in the quotient P_K/Q_K . Spectra averaging plus Padé-based extrapolation yield more sharply delineated pole-zero coincidences compared to the case without averaging and extrapolation, thereby improving signal-noise ratios [37].

The SNS concept is illustrated in Figure 4, which shows the reconstructed poles and zeros [panel A] and magnitudes [panel B]. Figure 4 shows that signal and noise are separated, as evidenced by the distributions of poles (circles) and zeros (dots) on panel A, as well as magnitudes on panel B. Blue and red circles indicate the parameters for genuine and spurious resonances, respectively. Spurious resonances are spotted by circle-dot (pole-zero) coincidences at negative imaginary frequencies [panel A] and zero-valued magnitudes [panel B]. The most clearly visualized SNS is in panel A, where signal and noise belong to two distinct regions, with positive and negative imaginary frequencies, respectively. An unphysical side of a spurious resonance is that its FWHM and T_2^* are both negative, as opposed to physical resonances for which $\text{FWHM} > 0$ and $T_2^* > 0$. The relation $\text{FWHM} \sim 1/T_2^*$ is visually interpretable from Figure 4A. Thus, for example, the pole of the genuine resonance NAA is deep within the positive imaginary part of the complex frequency plane, reflecting a wider resonance with fast decay. The pole of acNeu is closer to the abscissa, consistent with a narrower peak, for which T_2^* is longer. The resonances in the lipid doublet at ~ 1.34 ppm are wide (large FWHM), their poles lying deeply at imaginary frequencies, as is the pole corresponding to macromolecule at ~ 3.7 ppm. These macromolecules decay rapidly, appearing with short TE, as in the present analysis. The genuine resonances have non-zero magnitudes [Figure 4B], albeit sometimes very small, such as phosphocholine and glycerophosphocholine at ~ 3.22 and 3.23 ppm, respectively. The lipid doublets at ~ 1.34 ppm have large magnitudes. The magnitude is even larger for NAA at ~ 2.03 ppm, while the magnitude of acNeu is smaller. The NAA peak is shorter and broader than acNeu on the total shape spectrum, as per Figure 1B, whereas the larger width of NAA compared to acNeu is seen in Figure 4A. This implies more attenuation of the magnitude of NAA than acNeu, since peak height is proportional to the ratio magnitude/FWHM. The findings for NAA and acNeu in Figures 4A and 4B are consistent with the total shape spectrum. The importance of quantification provided by the FPT, yielding the component shape spectra [Figure 2B and Figure 3B] from the reconstructed parameters is seen.

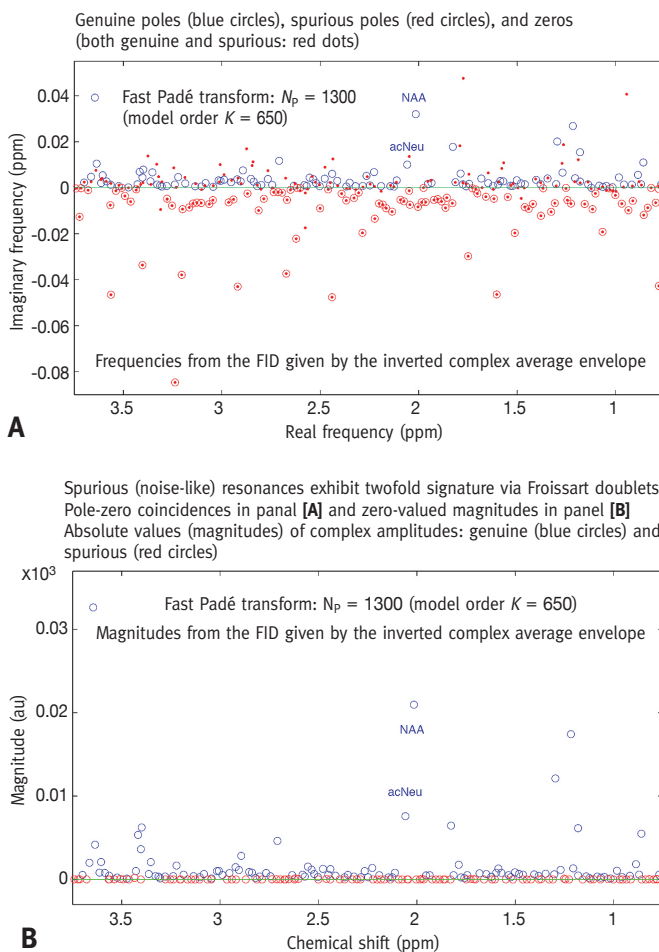
CLINICAL IMPLICATIONS OF THE FINDINGS FOR PADÉ-OPTIMIZED IN VIVO MRS FROM THE OVARY

The Padé-based strategy for processing in vivo MRS time signals has been validated for MRS data from the brain, from

at the roots of $Q_K = 0$. Complex amplitudes have different but complementary meanings in the time and frequency domains. In the time domain, amplitudes are the intensity of oscillations of damped, sinusoidal waveforms. In the frequency domain, amplitudes are the strength of the poles in the spectrum P_K/Q_K . Pole-zero parameterization sets the stage for SNS. False information is identified by a pair of identical unstable poles and zeros (Froissart doublets) yielding zero amplitudes. The latter is due to amplitude being directly proportional to pole-zero distance. True information is recognized as stable, with non-coincident

which very dense spectra were engendered [34,35]. This Padé methodology is also validated for in vivo encoded MRS data from the ovary. A key aspect of the FPT for in vivo encoded MRS time signals is spectra averaging [35], in which the arithmetic average is taken of a pre-computed sequence of the retrieved envelopes. Spectra averaging stabilizes the total shape spectra that are highly sensitive to model order K . Without averaging, large spikes are generated for envelopes reconstructed with a sequence of values of K . Averaging these envelopes engenders a total shape spectrum void of spikes, which illustrates the random, noise-like nature of spurious resonances with change in K . Averaging of spectra is not possible in the FFT because Fourier vectors in the frequency domain are not of the same length for different truncation of the total acquisition time T [35]. However, as a general procedure, spectra averaging could be useful for other parametric processors, such as those reviewed by Belkić [29]. Spectra averaging is one aspect of the noise suppressing capabilities associated with the FPT. Separation of genuine from spurious content, based on pole-zero coincidence and zero or near zero magnitudes is also provided by the FPT. Through a variant of the FPT used here (genuine and spurious poles at positive and negative imaginary frequencies, respectively), yet another way is provided to cast out noisy content, while identifying true metabolites [30]. Insight was gleaned from the real part of the complex average envelope. This real total shape spectrum is very dense, due to encoding at short TE, such that short-lived metabolites had not yet decayed. Interpretation of such a dense spectrum is a major challenge. Queries include: What is the relative abundance of each identified metabolite? Could there be even more resonances hidden beneath the large structures? Without parametric analysis, the answers to these questions cannot be ascertained. It is vital to proceed beyond total shape spectra to analyze spectral components, via the parametric FPT, whereby all genuine resonances are identified and peak parameters precisely computed. Clarification emerges from parametric analysis. In the chemical shift region ~ 1.3 ppm, the component spectra clarify the overlap among lipid, lactate, threonine and other resonances. These insights may help resolve uncertainty as to whether the presence of lipids distinguishes benign from cancerous lesions. Although lipid at 1.3 ppm was more often identified in malignant lesions, this difference was not statistically significant in our meta-analysis [22]. Conversely, in our meta-analysis, lactate also at 1.3 ppm was found to be significantly associated with cancerous as opposed to benign ovarian lesions, but data regarding lactate were sparse. The key to clarification is to perform Padé-based parametric analysis using a short TE because then lipid, lactate, and other metabolites around 1.3 ppm can be identified and quantified. In the chemical shift region ~ 2.0 ppm, there have also been uncertainties that obscure interpretation of MR spectra from the ovary. Via Padé reconstructions, the

Figure 4. In vivo MRS for ovarian tumor: Padé-retrieved genuine and spurious parameters. Signal-noise separation or SNS by the FPT. Complete separation of genuine from spurious frequencies [A], with open circles for poles and dots for zeros. The genuine and spurious poles are shown in blue and red circles, respectively. In [B], the magnitude plot shows zero-valued magnitudes of spurious resonances (red circles), and non-zero magnitudes for genuine resonances (blue circles)



Au = arbitrary units, FPT = fast Padé transform, MRS = magnetic resonance spectroscopy, FID = free induction decays (metabolite abbreviations above the two centrally located peaks: NAA = N-acetyl aspartate, acNeu = N-acetylneuraminic acid)

two resonances between 2.0 and 2.1 ppm corresponding to NAA and acNeu were unambiguously distinguished, such that it is possible to ascertain the actual significance of NAA versus acNeu for distinguishing cancerous from benign ovarian lesions. Not only was choline at 3.2 ppm identified and its peak parameters reconstructed via the FPT, for the first time, phosphocholine and glycerophosphocholine, were also detected from in vivo MRS of the ovary. The genuine nature of the PC and GPC resonances was confirmed by their positive imaginary frequencies, lack of pole-zero coincidence and non-zero, albeit small, magnitudes. Yet another confirmation of the physical nature of these two resonances was stability of

their spectral parameters. Notably, since phosphocholine is identified as an indicator of malignant transformation [27,28], it becomes possible via the FPT to non-invasively assess this biomarker. With post-processing fitting of FFT-generated spectra, dense spectra are problematic and, thus, encoding is preferred at longer TEs for computing sparser, simpler spectra [35]. Via the FPT, use of short TEs becomes feasible to detect rapidly decaying metabolites. To tap into this information, the signal processing method must reliably disentangle overlapping resonances. The parametric FPT is fully capable of this task, as seen herein, and in other studies [22,29-35,37].

FUTURE PERSPECTIVES

The ovary is a small, moving organ, such that encoding good quality MRS time signals is technically challenging [22,36]. This difficulty plus meager results from Fourier-based in vivo MRS of the ovary, have undoubtedly put a damper on efforts to explore MRS for early ovarian cancer detection. Thus, the MR community has not prioritized this problem area. The present results indicate that this situation can and should change. There is now justification to further apply Padé-optimized in vivo MRS (FPT-MRS) for early ovarian cancer detection and better identification of benign ovarian lesions. The next steps would be to apply the FPT to in vivo MRS time signals encoded from different ovarian cancer types, benign ovarian lesions and normal ovary. Given the heterogeneity of ovarian pathology, this task will require extensive multivariate exploration to ascertain the metabolite patterns that most robustly distinguish benign from borderline or clearly cancerous ovary. The anticipated enhanced diagnostic accuracy, plus shortened examination time for the patient provided by FPT-MRS [32] would improve cost-effectiveness. Overall, software upgrades with unbiased quantifying signal processing, such as the FPT, are indispensable for achieving these long-sought goals in the clinic. Lack of ionizing radiation exposure with MR-based methods is a key advantage. Of note, diagnostic radiation may be particularly deleterious for women at high risk for ovarian cancer [38]. For women with an elevated ovarian cancer risk due to heredity, ionizing radiation exposure, or other risk factors, FPT-MRS could be useful for surveillance. Women themselves have expressed an interest and preference for screening surveillance strategies vis-à-vis ovarian cancer [12,39,40]. Critically, early ovarian cancer detection would markedly improve survival for women afflicted with this malignancy. Effective diagnostic methods are needed to achieve this aim, to which in vivo FPT-MRS is expected to contribute.

Acknowledgements

This work was supported by the Marsha Rivkin Center for Ovarian Cancer Research, King Gustav the 5th Jubilee Fund, and the fund for research, development and education (FoUU) of the Stockholm County Council.

We would like to thank our colleagues, Professors Marinette van der Graaf, Leon Massuger, Ron Wevers, Eva Kolwijck, Udo Engelke, Arend Heerschap, Henk Blom, M'Hamed Hadfoune, and Wim Buurman from Radboud University for making the in vivo encoded magnetic resonance spectroscopy time signals available to us.

Correspondence

Dr. K. Belkić
Dept. of Oncology-Pathology, Karolinska Institute, Stockholm SE-17176 Sweden
Phone: (46-8) 5177-2184
email: Karen.Belkic@ki.se

References

1. Global Burden of Disease Cancer Collaboration. The Global Burden of Cancer 2013. *JAMA Oncol* 2015; 1: 505-27.
2. Malvezzi M, Carioli G, Rodriguez T, Negri E, La Vecchia C. Global trends and predictions in ovarian cancer mortality. *Ann Oncol* 2016; 27 (11): 2017-25.
3. Anton-Culver H, Chang J, Bray F. Cancer burden in four countries of the Middle East Cancer Consortium (Cyprus; Jordan; Israel; Izmir (Turkey)) with comparison to the United States surveillance, epidemiology and end results program. *Cancer Epidemiol* 2016; 44: 195-202.
4. Gabai-Kapara E, Lahad A, Kaufman B, et al. Population-based screening for breast and ovarian cancer risk due to BRCA1 and BRCA2. *Proc Natl Acad Sci U S A* 2014; 111: 14205-10.
5. Chornokur G, Armankwah E, Schildkraut J, Phelan C. Global ovarian cancer health disparities. *Gynecol Oncol* 2013; 129: 258-64.
6. Morgan R, Armstrong D, Alvarez R, et al. Ovarian cancer, version 3.2012 featured updates to the NCCN guidelines. *J Natl Compr Canc Netw* 2012; 10: 1339-49.
7. Seidman J, Wang B. Evaluation of normal-sized ovaries associated with primary peritoneal serous carcinoma for possible precursors of ovarian serous carcinoma. *Gynecol Oncol* 2007; 106: 201-6.
8. Andersen M, Lowe K, Goff B. Value of symptom-triggered diagnostic evaluation for ovarian cancer. *Obstet Gynecol* 2014; 123: 73-9.
9. Jacobs I, Menon U, Ryan A, et al. Ovarian cancer screening and mortality in the UK Collaborative Trial of Ovarian Cancer Screening (UKCTOCS): a randomised controlled trial. *Lancet* 2016; 387: 945-56.
10. Partridge E, Greenlee R, Riley T, et al. Assessing the risk of ovarian malignancy in asymptomatic women with abnormal CA 125 and transvaginal ultrasound scans in the Prostate, Lung, Colorectal, and Ovarian Screening Trial. *Obstet Gynecol* 2013; 121: 25-31.
11. Moyer V. Screening for ovarian cancer: U.S. Preventive Services Task Force reaffirmation recommendation statement. *Ann Intern Med* 2012; 157: 900-4.
12. Belkić K, Cohen M, Márquez M, et al. Screening of high-risk groups for breast and ovarian cancer in Europe: a focus on the Jewish population. *Oncol Rev* 2010; 4: 233-67.
13. Morgan R, Alvarez R, Armstrong D, et al. Ovarian cancer, version 1.2016 clinical practice guidelines in oncology. *J Natl Compr Canc Netw* 2016; 14: 1134-63.
14. Hartmann L, Lindor N. The role of risk-reducing surgery in hereditary breast and ovarian cancer. *N Engl J Med* 2016; 374: 454-68.
15. Yerushalmi R, Rizel S, Zoref D, et al. A dedicated follow-up clinic for BRCA mutation carriers. *IMAJ* 2016; 18: 549-52.
16. Grossman SG. The Angelina Jolie effect in Jewish law: prophylactic mastectomy and oophorectomy in BRCA carriers. *Rambam Maimonides Med J* 2015; 6 (4).
17. Söletormos G, Duffy M, Othman Abu Hassan S, et al. Clinical use of cancer biomarkers in epithelial ovarian cancer: updated guidelines from the European Group on Tumor Markers. *Int J Gynecol Cancer* 2016; 26: 43-51.
18. Imaoka I, Araki T, Takeuchi M. MRI of the female genitourinary tract. In: Belkić DŽ, Belkić K (eds.) *Magnetic Resonance Imaging and Spectroscopy*, Volume 3, Comprehensive Biomedical Physics. Amsterdam: Elsevier, 2014: 221-40.
19. Kinkel K, Lu Y, Mehdizade A, Pelte M-F, Hricak H. Indeterminate ovarian mass at US: incremental value of second imaging test for characterization. *Radiology* 2005; 236: 85-94.
20. Djokić Kovač J, Terzić M, Mirković M, Banko B, Djikić-Rom A, Maksimović R. Endometrioid adenocarcinoma of the ovary: MRI findings with emphasis on diffusion-weighted imaging for the differentiation of ovarian tumors. *Acta Radiol* 2016; 57: 758-66.
21. Kircher MF, Hricak H, Larson SM. Molecular imaging for personalized cancer care. *Molecular Oncol* 2012; 6: 182-95.

22. Belkić Dž, Belkić K. In vivo magnetic resonance spectroscopy for ovarian cancer diagnostics: quantification by the fast Padé transform. *J Math Chem* 2017; 55: 349-406.
23. Kolwijck E, Engelke UF, van der Graaf M, et al. N-acetyl resonances in in vivo and in vitro NMR spectroscopy of cystic ovarian tumors. *NMR Biomed* 2009; 22: 1093-9.
24. Boss EA, Moolenaar SH, Massuger LF, et al. High-resolution proton nuclear magnetic resonance spectroscopy of ovarian cyst fluid. *NMR Biomed* 2000; 13: 297-305.
25. Kolwijck E, Wevers RA, Engelke UF, et al. Ovarian cyst fluid of serous ovarian tumors contains large quantities of the brain amino acid N-acetylaspartate. *PLOS One* 2010; 5 (4): e10293.
26. Abramov Y, Carmi S, Anteby SO, Ringel I. Ex vivo 1H and 31P magnetic resonance spectroscopy as a means for tumor characterization in ovarian cancer patients. *Oncol Rep* 2013; 29: 321-8.
27. Iorio E, Mezzanzanica D, Alberti P, et al. Alterations of choline phospholipid metabolism in ovarian tumor progression. *Cancer Res* 2005; 65: 9369-76.
28. Glunde K, Jiang J, Moestue SA, Gribbestad IS. MRS/MRSI guidance in molecular medicine: targeting choline and glucose metabolism. *NMR Biomed* 2011; 24: 673-90.
29. Belkić Dž. Quantum Mechanical Signal Processing and Spectral Analysis, Bristol: Institute of Physics Publishing, 2004: 56-72, 358-74.
30. Belkić Dž, Belkić K. Signal Processing in Magnetic Resonance Spectroscopy with Biomedical Applications. London: Taylor & Francis Publishers, 2010: 40-56, 138-48, 200-5, 228-49, 264-72, 311-30, 339-70.
31. Belkić Dž, Belkić K. Mathematical modeling applied to an NMR problem in ovarian cancer detection. *J Math Chem* 2008; 43: 395-425.
32. Belkić Dž, Belkić K. Strategic steps for advanced molecular imaging with magnetic resonance-based diagnostic modalities. *Technol Cancer Res Treat* 2015; 14: 119-42.
33. Belkić Dž, Belkić K. How the fast Padé transform handles noise for MRS data from the ovary: importance for ovarian cancer diagnostics. *J Math Chem* 2016; 54: 149-85.
34. Belkić Dž, Belkić K. Improving the diagnostic yield of magnetic resonance spectroscopy for pediatric brain tumors through mathematical optimization. *J Math Chem* 2016; 54: 1461-513.
35. Belkić Dž, Belkić K. Iterative averaging of spectra as a powerful way of suppressing spurious resonances in signal processing. *J Math Chem* 2017; 55: 304-48.
36. Massuger LFAG, van Vierzen PBJ, Engelke U, et al. H-Magnetic resonance spectroscopy: a new technique to discriminate benign from malignant ovarian tumors. *Cancer* 1998; 82: 1726-30.
37. Belkić Dž, Belkić K. Synergism of spectra averaging and extrapolation for quantification of in vivo MRS time signals encoded from the ovary *J Math Chem* 2017; 55 (5):1067-109.
38. Harlap S, Olson SH, Barakat RR, et al. Diagnostic X-rays and risk of epithelial ovarian carcinoma in Jews. *Ann Epidemiol* 2002; 12: 426-34.
39. Lux MP, Ackermann S, Nestle-Krämling C, et al. Use of intensified early cancer detection in high-risk patients with familial breast and ovarian cancer. *Eur J Cancer Prev* 2005; 14: 399-411.
40. Pavlik E, van Nagell JR Jr. Ovarian cancer screening-what women want. *Int J Gynecol Cancer* 2012; 22: S21-3.

Capsule

A brainy treatment for heart failure

Respiratory difficulty and diaphragm weakness are known symptoms of heart failure, but they are usually attributed to pulmonary edema damaging the diaphragm through physical stress. Foster and co-authors found that this is not the only contributing factor. In mouse models, diaphragm weakness developed even in heart failure without pulmonary edema. The authors linked this observation to changes in

angiotensin II and β -adrenergic signaling, which result in centrally controlled ventilatory overdrive. Drugs targeting β -adrenergic signaling were effective in preventing ventilatory overdrive and subsequent diaphragmatic injury, but only if they penetrated the blood-brain barrier.

Sci Transl Med 2017; 9: eaag1303
Eitan Israeli

Capsule

No safe haven for metastases

Although targeted therapies for cancer offer great promise, they are often much less effective against brain metastases than against peripheral tumors. This effect is generally attributed to the drugs' difficulty in penetrating the blood-brain barrier. Kodack et al. discovered that, at least in breast cancer that has spread to the brain, the brain micro-environment itself plays a role in treatment resistance. In mouse models

and human cancer samples, human epidermal growth factor receptor 3 (HER3) expression increased in breast cancer-associated brain lesions. The HER3 facilitated the tumors' survival in the presence of targeted treatment. Thus, inhibiting HER3 could help overcome tumor resistance to therapy.

Sci Transl Med 2017; 9: eaal4682
Eitan Israeli

“We must realise that man's nature will remain the same so long as he remains man; that civilisation is but a slight coverlet beneath which the dominant beast sleeps lightly and ever ready to awake. To preserve civilisation, we must deal scientifically with the brute element, using only genuine biological principles”

H. P. Lovecraft (1890–1937) American author who achieved posthumous fame through his influential works of horror fiction. He was virtually unknown and published only in pulp magazines before he died in poverty, but he is now regarded as one of the most significant 20th-century authors in his genre